Rapid full-color serial sectioning tomography with speckle illumination and ultraviolet excitation

Check for updates

Wentao Yu, Yan Zhang, Claudia T. K. Lo, Lei Kang & Terence T. W. Wong ✉

Three-dimensional (3D) high-resolution large-volume imaging has remained a challenge. Translational rapid ultraviolet-excited sectioning tomography (TRUST) achieves rapid and cost-effective whole-organ subcellular imaging through iterative optical scanning and mechanical sectioning. However, the axial resolution is limited by the mechanical sectioning thickness or the UV light penetration depth in tissue. Here, assisted with high-and-low-frequency (HiLo) microscopy (HiLoTRUST), the optical sectioning thickness has been reduced from tens of micrometers to ~5.8 μm. In addition, HiLoTRUST has attained a finer mechanical sectioning thickness (10–15 μm) compared to TRUST (50 μm). For high-content imaging as in TRUST, we employed two additional UV light-emitting diodes (LEDs) specifically for uniform illumination. The full-color imaging ability and improved axial resolution of HiLoTRUST have been validated by two-dimensional (2D)/3D imaging of various mouse organs and human lung cancer specimens. HiLoTRUST offers a cost-effective, full-color, and high-resolution 3D imaging approach, showing its great potential in 3D histology applications.

Two-dimensional (2D) slide imaging offers detailed information about planar morphology and anatomical structures of tissues and cells, yet it fails to visualize the comprehensive internal three-dimensional (3D) structural information or spatial correspondence, which can be crucial for cancer diagnosis[1,2] or embryonic development study[3]. Conventional 3D histology can be exceedingly labor-intensive and time-consuming, as it involves manually sectioning and staining thousands of thin tissue slices to avoid light scattering or tissue absorption[4]. Moreover, a sophisticated image registration algorithm is necessary to restore the lost relative spatial information among different sections[5,6]. Regarding this, various automated 3D optical imaging techniques have emerged and can be broadly categorized into two groups. The first category employs tissue clearing to significantly reduce light propagation issues in biological tissue[7–9]. As a representative example, light-sheet fluorescence microscopy (LSFM)[10] is typically combined with tissue clearing for rapid and non-destructive whole-organ imaging. Despite significant achievements, both tissue clearing and LSFM are still under development. Tissue clearing must balance the clearing effect and time expenditure to prevent tissue degradation, especially for large samples, while LSFM needs to balance imaging resolution and volume[11].

The second group relies on block-face serial sectioning tomography (BSST) to expand the imaging volume, where scanning is only required for the tissue block's surface layer in each round[12–15]. Although this sectioning procedure is destructive, BSST generates inherently aligned images, and its imaging volume can be relatively easily scaled up through simple modifications to the sectioning system. Block-face imaging in BSST systems depends on the optical sectioning capabilities of the specific light microscopy applied (e.g., spinning disk-based confocal microscope[16]). Consequently, while straightforward in principle, the overall complexity of BSST systems can still be high, particularly when multicolor imaging is needed. Moreover, many BSST systems require whole-mount staining and embedding of imaged samples in hard supporting materials (e.g., resin or paraffin), which adds time and labor costs and induces noticeable tissue shrinkage due to dehydration[17,18].

To this end, we previously introduced a whole-organ/embryo imaging method called translational rapid ultraviolet-excited sectioning tomography (TRUST)[11]. TRUST achieves an exceptional balance in time efficiency, imaging resolution, and cost-effectiveness by enjoying the benefits of ultraviolet (UV) surface excitation[19] and real-time staining with fluorogenic dyes[20]. TRUST accomplishes optical sectioning by taking advantage of the shallow penetration of deep UV light in tissue. Therefore, imaging axial resolution and contrast can considerably deteriorate when the light penetration depth is significantly larger than the objective lens's depth of field (DOF). This can occur when imaging tissue with relatively low scattering properties (e.g., human breast, ~100 μm UV penetration depth[21]) or when

Translational and Advanced Bioimaging Laboratory, Department of Chemical and Biological Engineering, The Hong Kong University of Science and Technology, Kowloon, Hong Kong, China.
✉e-mail: ttwwong@ust.hk

using a high-magnification objective lens[22]. In addition, the coarse sectioning thickness (50 μm) in TRUST worsens axial resolution and leads to tissue information loss, as certain tissue layers might not be exposed to the imaging system.

To address these issues, we present HiLoTRUST, which integrates the high-and-low-frequency (HiLo) microscopy[23] into TRUST for better optical sectioning capability and imaging contrast by rejecting the out-of-focus fluorescence background. Unlike other structured illumination microscopy (SIM)-based widefield optical sectioning methods, HiLo only requires two shots per field of view (FOV): one captured under speckle illumination and another under uniform illumination. Furthermore, compared to patterned illumination techniques, this approach is more robust against aberrations or scattering in tissues due to the statistically invariant of fully developed speckles[24]. Also, HiLoTRUST utilizes a finer sectioning thickness (10–15 μm) to enhance tissue continuity in the axial direction, resulting in more accurate and detailed 3D image reconstruction (Supplementary Figure 1).

To retain the full-color imaging capability of TRUST, we have also developed full-color HiLo microscopy, which offers improved color contrast and more information compared to conventional monochrome HiLo microscopy. Although we have previously proposed dual-channel HiLo microscopy for 2D histological imaging, it relies on sequential channel imaging at the expense of acquisition time[25]. Full-color HiLo microscopy employs deep UV light-emitting diodes (LEDs) for uniform illumination, allowing the excitation of labeled stains and endogenous tissue components (Supplementary Figure 2). The resulting fluorescence signals can be simultaneously captured by the integrated color camera. For speckle illumination, a green 532 nm laser diode (LD) is used, and a notch filter (NF) at 532 nm serves as the excitation bandstop filter while permitting most of the visible spectra to pass. Unlike traditional illumination mode switching methods (i.e., uniform or speckle illumination) that depend on mechanical high-speed scanning with a galvanometer[24] or rotating the diffuser[25], HiLoTRUST uses a microcontroller unit for illumination light sources and mode switching. This low-cost electronic approach eliminates potential system vibration and lengthy start-stop times associated with mechanical methods.

To evaluate the effectiveness and reliability of full-color HiLo microscopy, we initially conducted 2D imaging on various mouse organs (e.g., liver, lung, kidney, and brain). We have also devised adapted HiLo processing pipelines for challenging situations where low-frequency non-nuclear structures may not be excited under speckle illumination. Then, we implemented 3D imaging with HiLoTRUST for mouse organs (e.g., kidney, lung, and liver), and compared the obtained 3D datasets with imaging results from TRUST, highlighting a superior optical sectioning capability. Finally, we captured images of two human lung cancer samples, showcasing HiLoTRUST's potential for clinical applications. In summary, HiLoTRUST offers a cost-effective, full-color, and high-resolution 3D imaging approach, holding great promise for 3D histology applications.

Results

Setup of the full-color HiLo microscopy

The schematic of the full-color HiLo microscopy for 2D block-face imaging is shown in Fig. 1a. To acquire the speckle illumination image (I_s), the 532 nm green LD is turned on, emitting the light beam with a diameter of 2 mm. After passing a 220-grit ground glass diffuser (DG10-220, Thorlabs Inc.), the generated speckle pattern is then relayed onto the back focal plane of the objective lens[25–27] (UPlanFL N 10× /0.3 numerical aperture (NA), RMS10X-PF, Olympus Corp.) by a pair of expansion lenses (L1 and L2, with focal lengths of 25 mm and 75 mm, respectively), forming a speckle pattern with an average grain size of ~4 μm. The side window length Λ is set as 10 μm when calculating the local contrast C_s. Subsequently, the fluorescence signals from the excited cell nuclei labeled with PI will be collected by the same objective lens. After passing the beam splitter (BS) (30 R:70 T, BSS10R, Thorlabs Inc.) and the 532 nm NF, the fluorescence signals will be focused on the color camera (DS-Fi3, Nikon Inc.) by an infinity-corrected tube lens

(TTL180-A, Thorlabs Inc.). The 532 nm NF positioned just before the tube lens (TL) functions as an excitation bandstop filter, allowing the majority of visible signals to pass through.

To transit to uniform illumination, the LD is turned off while the two mounted deep UV-LEDs (~ 285 nm, M285L4, Thorlabs Inc.) are activated simultaneously. Dual UV-LEDs are applied for high illumination energy and uniformity. The UV light beams are roughly focused on the surface of the specimen by two pairs of lenses (#67-270, Edmund Optics Inc.; LA4306-UV, Thorlabs Inc.) with an oblique orientation. The excited fluorescence signals will be collected by the objective lens and propagate back following the same optical path as it is in speckle illumination. The narrow bandwidth of the 532 nm NF (~ 10 nm) allows the transmission of most fluorescence signals in the visible spectrum, enabling full-color imaging (Supplementary Figure 3). The results in Fig. 1b–g present an intuitive example to better illustrate the principles of full-color HiLo microscopy. Figure 1b,c are two shots (i.e., I_s and I_u) acquired under speckle illumination with LD and uniform illumination with UV-LEDs, respectively. Under speckle illumination, only PI-labeled cell nuclei can be excited. Because the emission spectrum presents a peak around 615 nm, the red channel of the acquired color image is extracted as the speckle illumination image I_s. The speckle contrast image C_s (Fig. 1d) is calculated following Eq. (4) to reject the out-of-focus low-frequency components in Fig. 1e, outputting only the in-focus low-frequency image I_{Lo} (Fig. 1f). Finally, the calculated in-focus high-frequency components (I_{Hi}) and in-focus low-frequency components (I_{Lo}) can be merged as the final output I_{HiLo} (Fig. 1g) based on Eq. (6).

HiLoTRUST system setup

The HiLoTRUST system is developed by integrating the 3-axis motorized stage (Motor-*xyz*, L-509.20SD00, PI miCos GmbH) and the vibratome (VF-500-0Z, Precisionary Instruments Inc.) into the full-color HiLo microscopy, as depicted in Fig. 2a. Prior to imaging, the specimen is translated near the objective lens for focusing. At the same time, the specimen is also near the wall of the water tank such that the gap between the objective lens and the tissue surface will be mostly filled with air instead of stains to minimize the fluorescence background arising from staining solutions. Part of the water tank near the objective lens is made of quartz, allowing transmission of both the UV illumination and the excited fluorescence signals in the visible wavelength range.

During imaging, two motorized linear stages (Motor-*x* and Motor-*y*) translate the specimen along the *x*–*y* plane for raster scanning when the FOV is insufficient to cover the entire section. An additional Motor-*z* is employed for focal scanning along the axial direction. After image scanning, Motor-*xyz* positions the specimen near the vibratome's blade for subsequent sectioning. The tissue sectioning thickness depends on the relative spatial position between the blade and the specimen. Hence, precise manual spatial localization of the translation stage is necessary during system alignment to guarantee sectioning accuracy. Once the system is calibrated, further experiments can proceed without manual recalibration, as the spatial positions are tracked by three custom limit switches attached to the motors (i.e., Motor-*x*, Motor-*y*, and Motor-*z*).

The entire 3D imaging part consists of repeatedly performing the first four steps shown in Fig. 2b: (1) fluorescent staining of the tissue's top layer for approximately 150 s, (2) widefield imaging using raster-scanning and focal scanning under speckle illumination by the LD, (3) widefield imaging using raster-scanning and focal scanning under uniform illumination by two deep UV-LEDs, and (4) removing the imaged layer with the vibratome to reveal the layer beneath. After HiLo image processing in Step (5), 3D reconstruction in Step (6) can be realized by direct image stacking because the produced image sections are inherently aligned.

The selected vibratome is capable of sectioning samples with diameters up to 20 mm, and if necessary, an alternative model (VF-800-0Z, Precision Instruments Inc.) can be employed to increase the sectioning diameter to 100 mm. We also modified the VF-500-0Z vibratome to enhance its compatibility with the HiLoTRUST system. For example, we replaced the

original water tank, which contained chemical solutions (DAPI and PI) for real-time staining, with a larger 3D-printed version to accommodate more space for 3D scanning and the placement of mechanical components such as the sample stage shown in Fig. 2a. Furthermore, we removed the original vibratome's sectioning thickness control unit and integrated another motorized stage (Motor-s: L-509.10SD00; PI miCos GmbH; not depicted in Fig. 2a) to regulate the sectioning thickness automatically by adjusting the sample stage's position, considering the blade's position remains fixed. To guarantee that the objective lens's focal plane aligns parallel to the sample surface defined by the vibratome's blade angle, we placed a custom-built 2-axis angle adjustable platform (adjusting pitch and roll, as seen in TRUST[11])

beneath the vibratome and used a commercial high-precision rotation mount (Rotator in Fig. 2a) to modify the yaw angle.

Validation of full-color HiLo microscopy

We initially evaluated the high-content and optical sectioning ability of the full-color HiLo microscopy by capturing 2D HiLo images (i.e., HiLoTRUST images) of various mouse organs (such as lung, kidney, liver, and brain) and comparing the results with widefield images (i.e., TRUST images), as illustrated in Fig. 3. The HiLo images (right half in Fig. 3a1–a4,b1–b4) display a significant improvement in image contrast compared to the widefield images (left half in Fig. 3a1–a4,b1–b4)
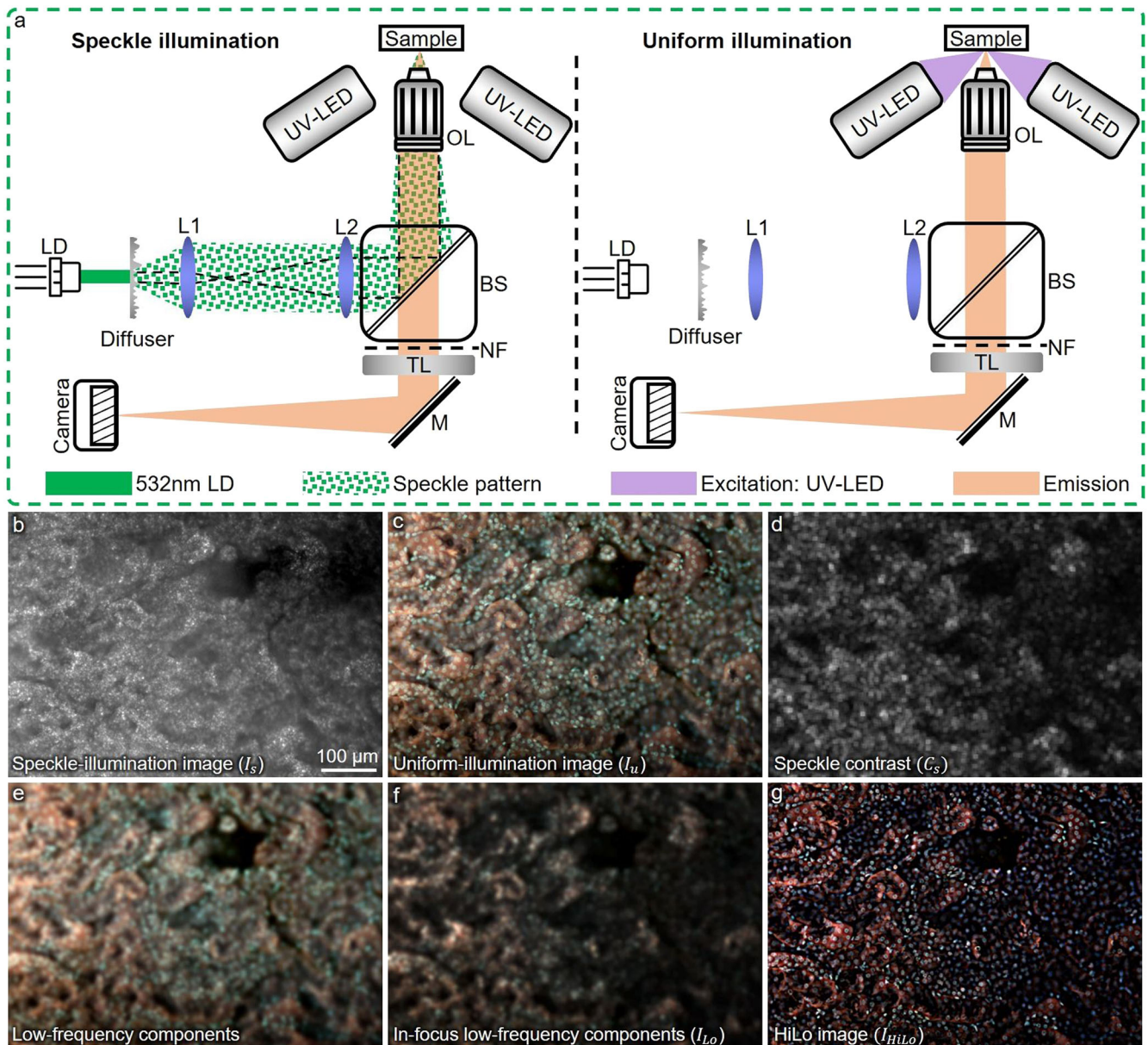

Fig. 1 | Illustrations of full-color HiLo microscopy. a Schematic of full-color HiLo microscopy. Two shots are required for each FOV. Under speckle illumination (left), the beam from the 532 nm laser diode is projected to the surface of the diffuser. The resulting speckle pattern is relayed to the back focal plane of the objective lens with a pair of expansion lenses, and finally projected onto the surface of the imaged sample. The excited fluorescence signals will then be collected by the objective lens, pass through the beam splitter, and finally be focused on the color camera. Under uniform illumination (right), the LD is powered off, and two UV-LEDs are activated, projecting UV beams obliquely from two slides. The fluorescence signals will follow the

same collection path as in the speckle image acquisition step. **b**–**g** An intuitive example illustrating the principles of full-color HiLo microscopy, where speckle illumination image (I_s), uniform illumination image (I_u), speckle contrast (C_s), in-focus low-frequency components (I_{Lo}), and the final output HiLo image (I_{HiLo}) of the same FOV of a mouse kidney is presented. LD, laser diode; L1, lens 1; L2, lens 2; OL, objective lens; BS, beam splitter; NF, notch filter; TL, tube lens; M, mirror. Note: images in **b**–**g** have been normalized with min-max normalization for better visualization.
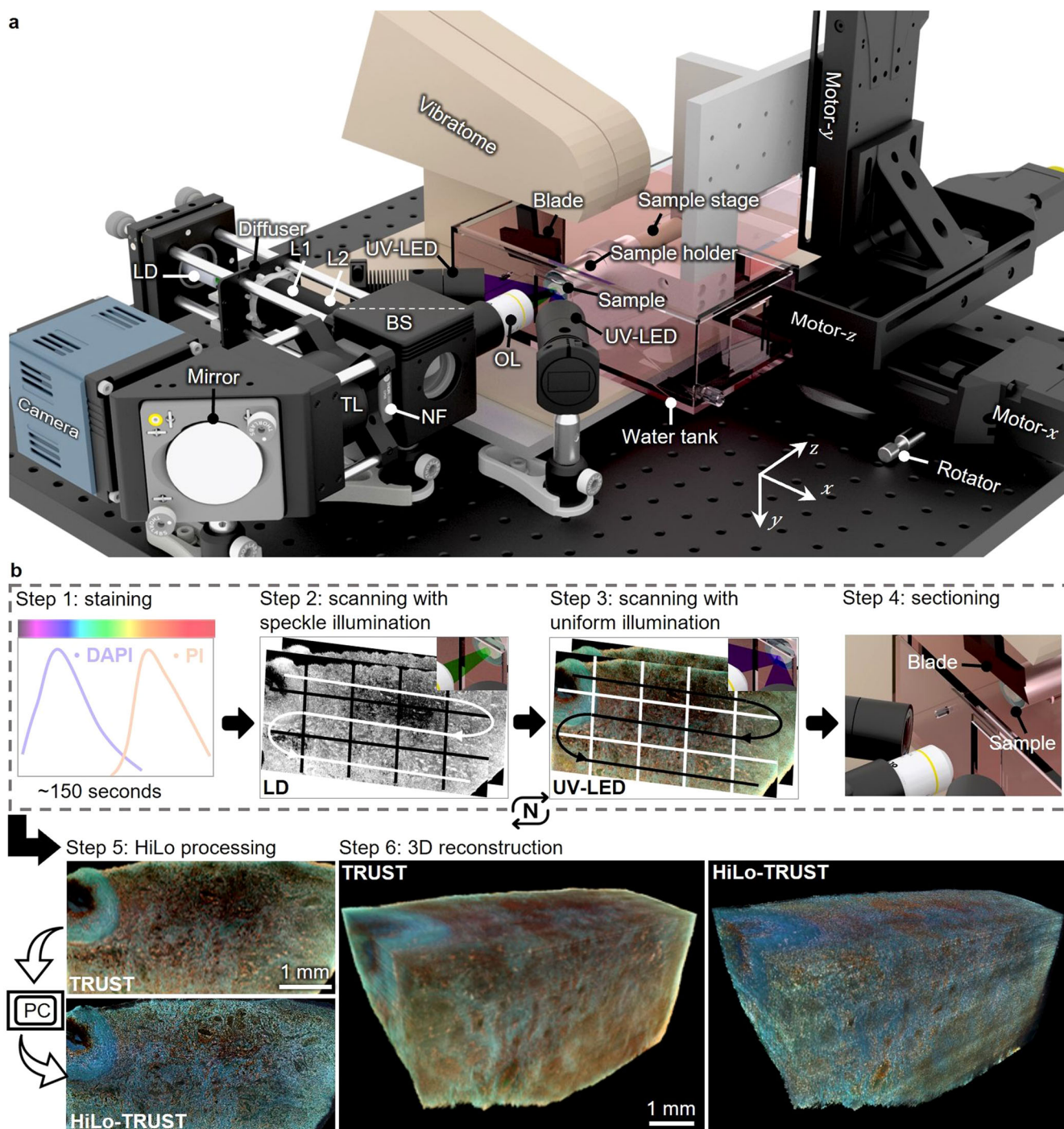
Fig. 2 | Overview of 3D imaging by HiLoTRUST. a Schematic of the HiLoTRUST system. **b** Workflow of the 3D imaging with HiLoTRUST, which contains six steps: (1) fluorescent staining with DAPI and PI for ~150 s, (2) widefield imaging with raster-scanning under speckle illumination by LD, (3) widefield imaging with raster-scanning under uniform illumination by two UV-LEDs, (4) shaving off the imaged layer with the vibratome to expose a layer underneath, (5) HiLo image processing, (6) 3D reconstruction by direct image stacking without image spatial registration. During imaging, the previous four steps will be repeated until the entire sample has been imaged and the whole procedure is fully automated with lab-built hardware and control programs. Note: TRUST and HiLoTRUST images have been normalized with min-max normalization for better visualization.

due to the reduction of out-of-focus background, which helps in identifying finer structures. Root mean square (RMS) contrast[28] was also computed for images in Fig. 3b1–b4, which shows a quantitative comparison of the image contrast. This feature is particularly important when dealing with highly transparent tissue samples, where the UV light's penetration depth may exceed the objective lens's DOF, resulting in reduced image contrast. For example, in the zoomed-in

image of lung tissue (Fig. 3b1), elastic fibers or alveoli exhibit increased clarity and distinguishability in the HiLo image (right) compared to the widefield image (left). Similarly, the nucleus in kidney tissue (Fig. 3b2), hepatocyte in liver tissue (Fig. 3b3), and nerve fibers in brain tissue (Fig. 3b4) all appear more distinct in the HiLo images (right) compared to the widefield images (left). As shown in Fig. 3c1–c4, we also conducted a quantitative analysis of the imaging contrast improvement by
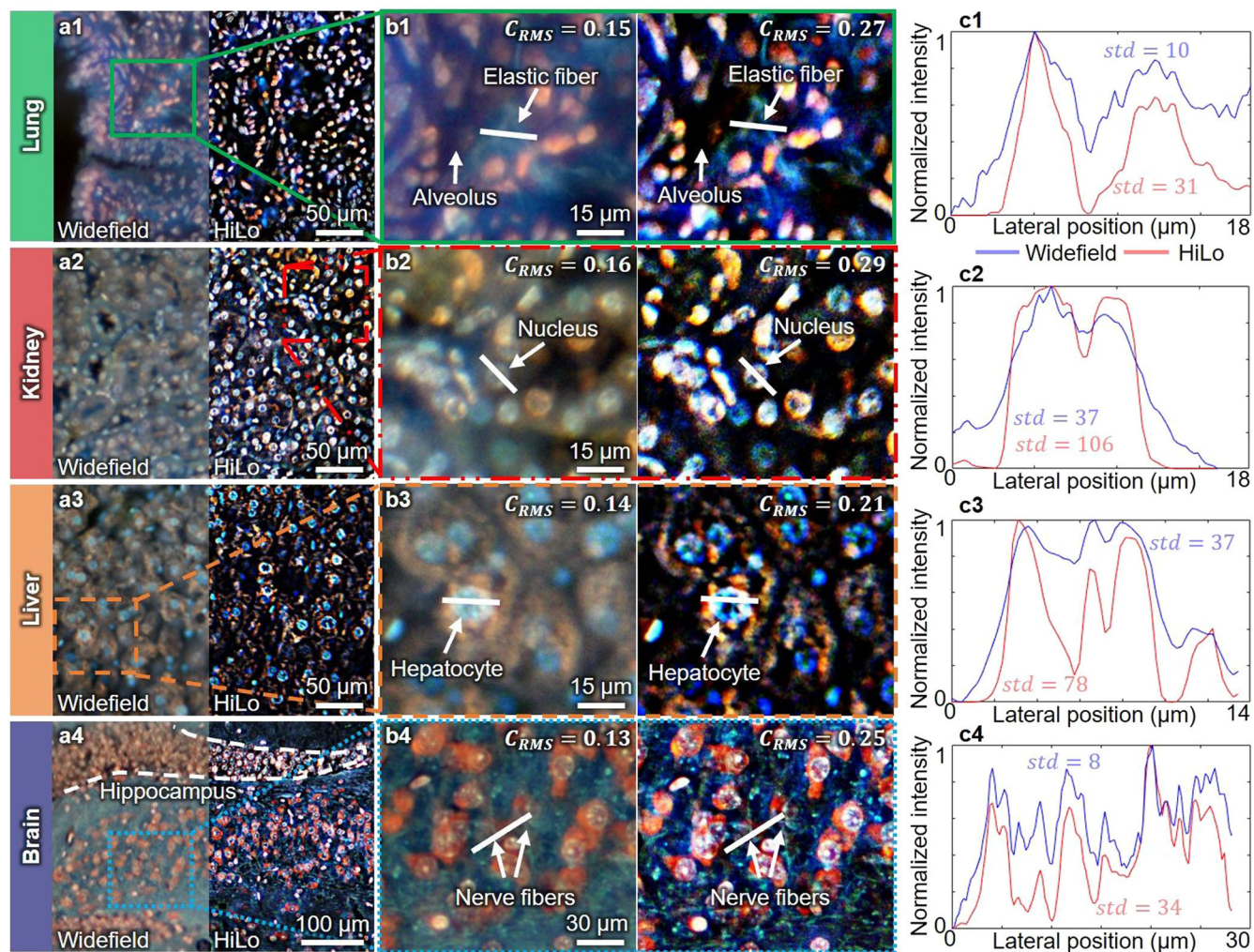
Fig. 3 | Experimental validation of full-color HiLo microscopy. a1–a4 Pairs of widefield images (left) and HiLo images (right) of mouse lung, kidney, liver, and brain tissue, respectively. **b1–b4** Zoomed-in pairs of TRUST images (left) and HiLoTRUST images (right) of the regions indicated in **a1–a4**. **c1–c4** Line profiles of solid white lines regions marked in **b1–b4** with min-max normalization, respectively. Note: widefield and HiLo images have been normalized with min-max normalization for better visualization (see Supplementary Figure 4 for HiLo images without normalization).

plotting the normalized intensity distributions along the solid white lines in Fig. 3b1–b4 and calculating the standard deviation (*std*) of the line profiles.

Under uniform illumination with UV-LEDs, autofluorescence signals from unlabeled components such as lipids, collagen, and fibers can also be excited and captured by the color camera[11], providing HiLoTRUST with high-content imaging capability. However, under speckle illumination with 532 nm LD, only the cell nucleus is excited. The speckle illumination image I_s (e.g., Fig. 1b) in HiLo microscopy is mainly used to generate the contrast image C_s (e.g., Fig. 1g) working as the weighting map to reject the out-of-focus background. Considering the dense distribution of cell nuclei and the current axial resolution achieved (~ 5.8 μm), the weighting map C_s based on cell nuclear information can be employed to evaluate the focusing status throughout the entire FOV in typical situations (e.g., Fig. 1b–g). Nonetheless, in regions where cell nuclear density is low and large non-nuclear components exist, C_s may not accurately represent the focus status. For instance, the hyaline cartilage shown in the widefield image (Fig. 4a, top) is not adequately represented in the corresponding HiLo image (Fig. 4a, bottom). To alleviate this challenging situation, we have modified the standard HiLo processing pipeline with two feasible solutions. The first method aims to mask out regions that HiLo processing is not suitable. The mask (Fig. 4c, top) is segmented based on its low-frequency property using the background removal plugin in ImageJ[29]. The resulting image (Fig. 4c,

bottom) retains the hyaline cartilage region while maintaining optical sectioning capability for other regions.

The second method involves selectively applying HiLo processing only in the color channel with the majority of fluorescence signals excited by speckle illumination (i.e., red channel, Fig. 4e, top). For other color channels, instead of HiLo processing, a high-frequency emphasis (HFE) filter[30] is applied, which preserves the low-frequency information content of the input image (I_{input}) while enhancing its high-frequency components. Note that compared to HiLo, HFE is also an image contrast enhancement technique but cannot effectively reject out-of-focus information as HiLo (Supplementary Figure 5). The resulting output image (I_{HFE}) can be described as:

$$I_{HFE}(\vec{r}) = \mathcal{F}^{-1}\left\{ \mathrm{a} + \mathrm{b} \cdot \mathcal{F}\left[I_{input}(\vec{r})\right] \times HP\left(\vec{k}\right) \right\} \qquad (1)$$

where $a \geq 0$ and $b > 1$. The outcome of combining HFE with HiLo processing is displayed in the bottom half of Fig. 4e by setting $a = 0.5$ and $b = 2$. To verify the versatility, the two adapted HiLo processing pipelines have also been applied to mouse brain tissue (Fig. 4b, d, f).

3D imaging with HiLoTRUST

It is important to note that, HiLoTRUST achieved a finer sectioning interval (~ 10 μm) by upgrading the vibratome model from VF-700-0z (used in
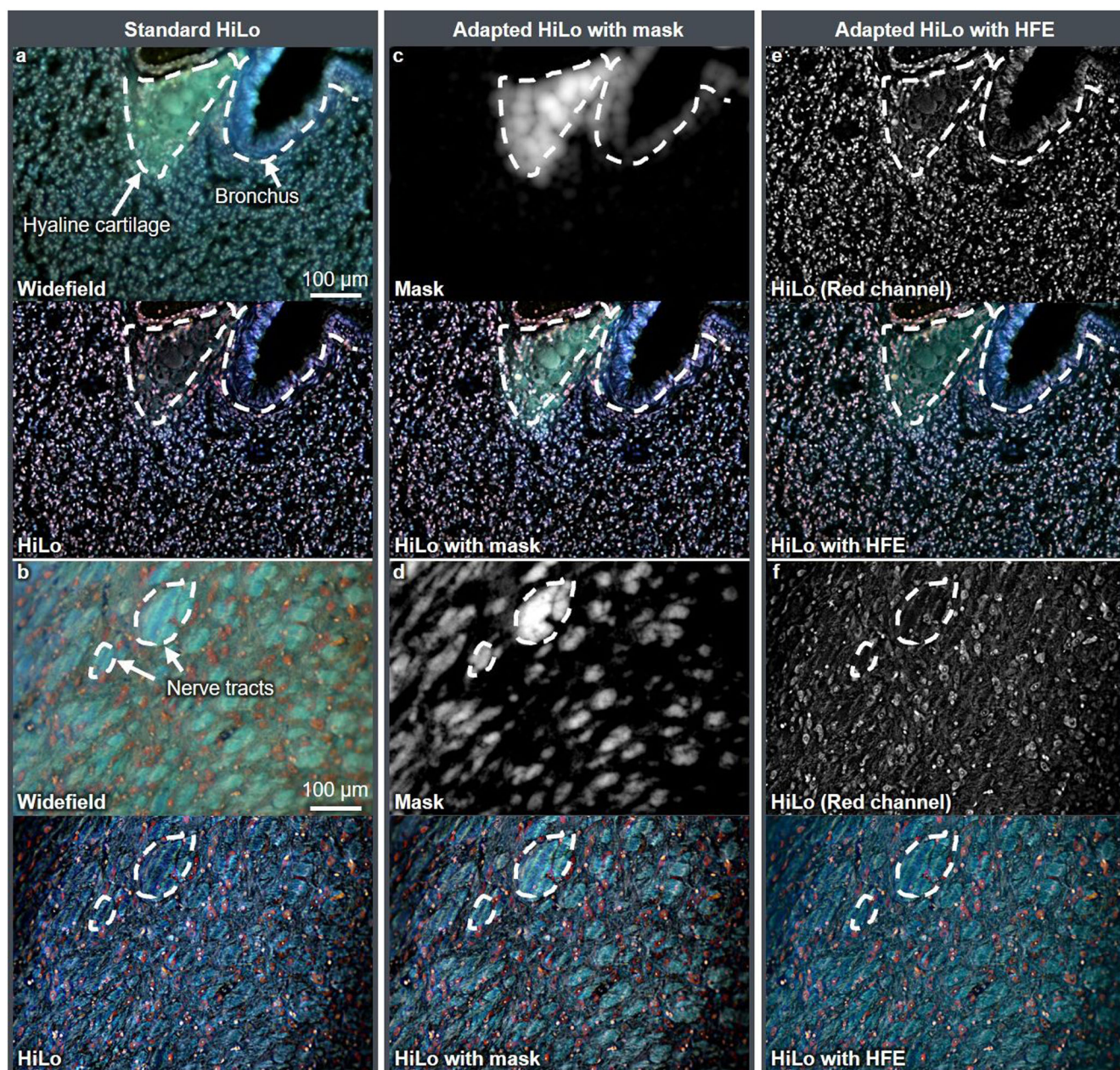
Fig. 4 | Adapted HiLo processing pipelines for challenging cases. a, b Two examples of challenging cases where directly applying standard HiLo processing is not appropriate. **c, d** The first adapted HiLo processing pipeline by masking out regions where standard HiLo processing is unsuitable. **e, f** The second adapted HiLo processing assisted with HFE. HFE, high-frequency emphasis. Note: widefield and HiLo images have been normalized with min-max normalization for better visualization.

TRUST) to VF-500-0z (used in HiLoTRUST) compared to the original TRUST (~ 50 μm). This improvement and additional focal scanning already resulted in better continuity along the axial direction for the reconstructed 3D image (Supplementary Figure 1). However, to make the comparison fair and emphasize the optical sectioning performance improvement of HiLoTRUST, the sectioning thickness and focal scanning parameters were set to be the same when acquiring TRUST or HiLoTRUST images in Fig. 5 and Fig. 6.

To assess the 3D imaging capability of HiLoTRUST, mouse kidney (Fig. 5a–c), lung (Fig. 5d–g, Supplementary Figure 6), and liver (Fig. 5h–j) tissue blocks were imaged. 2D/3D results of the same tissue block acquired with TRUST and HiLoTRUST are compared to demonstrate the enhanced imaging contrast achieved through HiLo processing. For example, Fig. 5b,c are 2D/3D zoomed-in images showing the vasa recta in the medulla region

marked with a solid green box in Fig. 5a, which serve as the countercurrent exchange system for solutes and water. Also, Fig. 5e,f are two close-up 2D image pairs of a mouse lung tissue, acquired with TRUST (top) and HiLoTRUST (bottom). Figure 5(g) is the rendered 3D model of a mouse lung tissue block imaged with TRUST (left) and HiLoTRUST (right), highlighting the significance of improved optical sectioning ability for tissue-level volumetric imaging. The 3D animation of the whole mouse lung block, including serial cross-sections, has also been rendered in Supplementary Movie 1. Finally, as shown in Fig. 5j, the vessel network in the liver tissue block (Fig. 5i) can be extracted based on the signal difference because their autofluorescence signal intensity is lower than that of the surrounding tissues[31,32]. With the trainable Weka segmentation plugin in Fiji[33], the vessel network can be segmented and the histogram of the vessel radius can be analyzed as in Fig. 5k with a mean value of 55 μm. It should be noted that
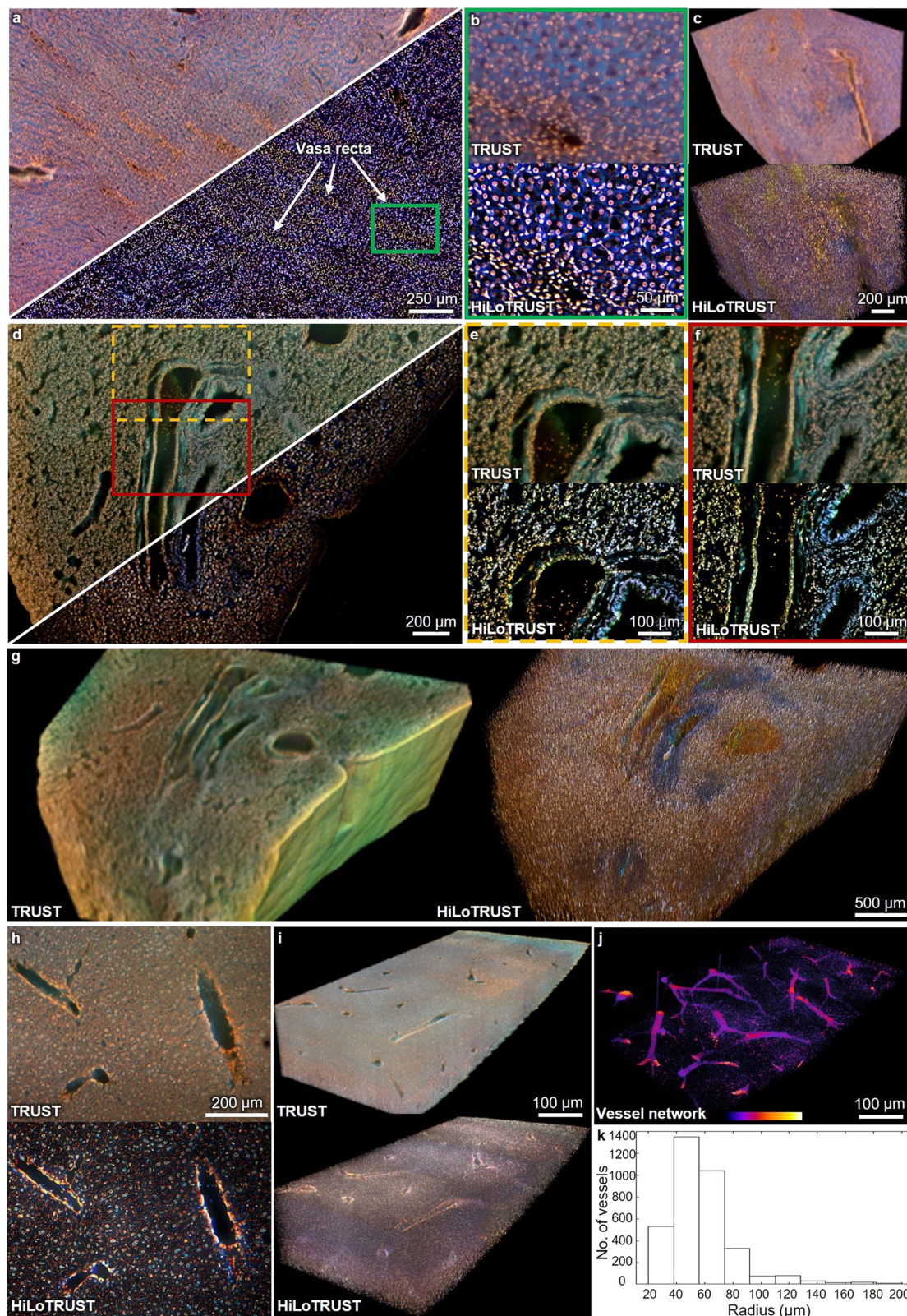
Fig. 5 | 2D/3D HiLoTRUST images of mouse organs. a 2D imaging results of the mouse kidney with TRUST (top left) and HiLoTRUST (bottom right). **b** Zoomed-in image comparison between TRUST (top) and HiLoTRUST (bottom) of the region in **a** marked with a solid green box. **c** Reconstructed 3D imaging results of the kidney tissue with TRUST (left) and HiLoTRUST (right). **d** 2D imaging results of the mouse lung with TRUST (top left) and HiLoTRUST (bottom right). **e, f** Close-up image comparisons between TRUST (top) and HiLoTRUST (bottom) of the region in **d** marked with a dashed orange box, and a solid red box, respectively.

g Reconstructed 3D imaging results of the lung tissue block with TRUST (left) and HiLoTRUST (right). **h** 2D imaging results of the mouse liver comparing TRUST (top) and HiLoTRUST (bottom). **i** Reconstructed 3D imaging results of the liver tissue block with TRUST (top) and HiLoTRUST (bottom). **j** The extracted vessel network from the same liver tissue block based on negative contrast. (**k**) The histogram of the vessel radius in **j**. Note: TRUST and HiLoTRUST images have been normalized with min-max normalization for better visualization.
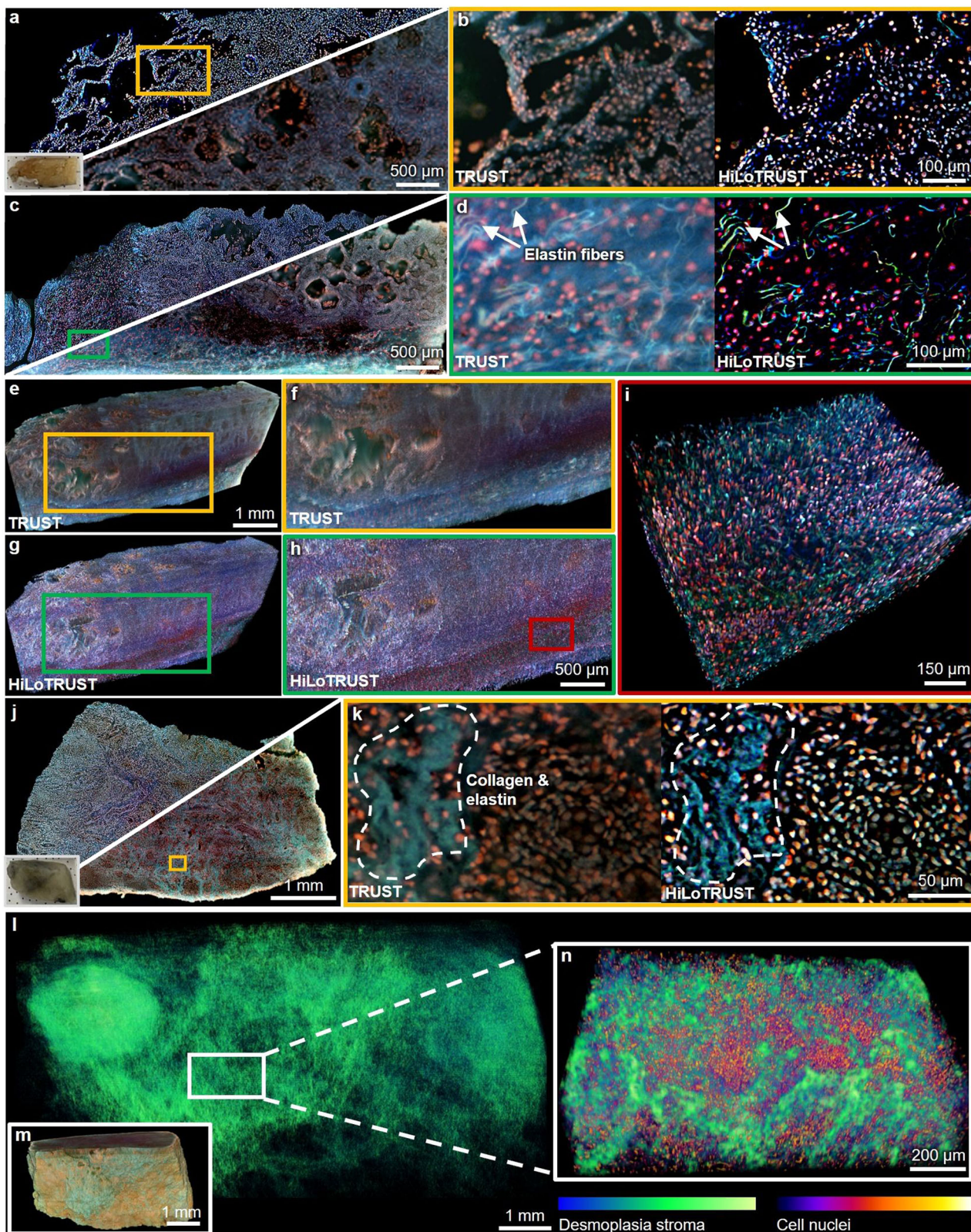
only relatively large vessels (> 20 μm in radius) have been successfully extracted, possibly due to the relatively low image contrast of vessels.

To demonstrate the potential of HiLoTRUST in clinical applications, imaging results of two human lung cancer specimens are presented in Fig. 6. Figure 6a shows the 2D imaging results of the lung specimen's cross-section layer from the first patient, with the top left half featuring the HiLoTRUST image and the bottom right half showcasing the TRUST image. Figure 6b offers a magnified comparison of the solid orange box region marked in Fig. 6a. Similarly, Fig. 6c depicts another cross-section layer of the same specimen. The magnified comparison in Fig. 6d demonstrates that the rejection of an out-of-focus background in HiLoTRUST significantly enhances the distinguishability of components such as elastin fibers, making them easier

Fig. 6 | 2D/3D HiLoTRUST images of human lung cancer specimens. a Cross-sectional imaging of the first specimen using HiLoTRUST (top left) and TRUST (bottom right). The inset at the bottom left shows a photograph of the specimen. **b** Zoomed-in TRUST image (left) and HiLoTRUST image (right) of the region in (a) marked with a solid orange box. **c** Another cross-section of the first specimen imaged with HiLoTRUST (top left) and TRUST (bottom right). **d** Zoomed-in TRUST image and HiLoTRUST image of the region in **c** marked with a solid green box. **e** 3D TRUST image of the first specimen. **f** Zoomed-in 3D TRUST image of the region marked by a solid orange box in **e. g** 3D HiLoTRUST image of the first specimen. **h** Zoomed-in 3D HiLoTRUST image of the region marked by a solid green box in **g. i** Zoomed-in 3D HiLoTRUST image of the region marked by a solid red box in **h.**

j Cross-sectional imaging with HiLoTRUST (top left) and TRUST (bottom right) of the second specimen. The inset at the bottom left shows a photograph of the specimen. **k** Zoomed-in TRUST image (left) and HiLoTRUST image (right) of the region in **j** marked with a solid orange box. **l** 3D distribution of the desmoplastic stroma extracted from the reconstructed 3D model in **m** utilizing color difference. **n** A magnified image of the solid white box region in (**l**) overlaid with nuclei within cells (predominantly cancer cells). This visualization provides an approximation of the 3D distribution relationship between collagen fibers and cancer cells. Note: TRUST and HiLoTRUST images have been normalized with min-max normalization for better visualization.

to identify. Figure 6e–i presents the comparison between TRUST and HiLoTRUST on 3D imaging. The zoomed-in result (Fig. 6i) of the region in Fig. 6h marked with the solid red box shows the clear 3D distribution of cells and fibers, providing evidence of the improved image contrast achieved by HiLoTRUST.

Similarly, Fig. 6j shows the 2D image of the lung specimen's surface layer from the second patient, acquired with HiLoTRUST (top left) and TRUST (bottom right). Figure 6k provides a magnified 2D comparison between TRUST and HiLoTRUST of the solid orange box marked in Fig. 6j. Due to the full-color imaging capability of HiLoTRUST, it is feasible to extract the 3D distribution of the desmoplastic stroma by utilizing color difference (i.e., green channel, Fig. 6l) based on the reconstructed 3D model in Fig. 6m. Figure 6n displays a zoomed-in view of the solid white box area in Fig. 6l, with cell nuclei superimposed, primarily from cancer cells. This visualization demonstrates the 3D distribution relationship between collagen fibers and cancer cells to some degree, showcasing HiLoTRUST's potential in cancer development research.

Discussion

In summary, TRUST has proven its potential in 3D histology or developmental study by whole-organ/embryo imaging. Here, regarding its limited axial resolution, we developed HiLoTRUST based on the full-color HiLo microscopy and have experimentally demonstrated that HiLoTRUST enables high-content full-color 3D imaging with subcellular resolution in a time- and cost-effective manner by the two-shot widefield illumination optical sectioning technique and the inexpensive light sources (i.e., green LD and a pair of UV-LEDs). To the best of our knowledge, this work demonstrates the first application of using HiLo microscopy assisted with deep UV surface excitation for full-color serial sectioning tomography. The improved performance has been validated by imaging diverse types of mouse organs (e.g., lung, liver, kidney, and brain). Moreover, human lung specimens with adenocarcinoma have also been imaged with the 3D distribution of desmoplasia stroma and cell nuclei being extracted, demonstrating its promising potential as a 3D histological imaging platform for clinical applications.

HiLoTRUST is still in its early development stage, and future research development can be conducted to further improve the performance of the system. The axial resolution of HiLo microscopy defined by FWHM has been reported to be less than 2 μm when imaging an optically thin sample[23]. To maintain acceptable in-focus speckle contrast, relatively large speckle patterns can be applied but at the cost of compromised axial resolution[25]. Even though the current axial resolution of ~5.8 μm is sufficient to produce an optical section comparable to a physical section in conventional slide-based histology.

One significant advantage of HiLoTRUST, when compared with other advanced 3D imaging systems (Supplementary Table 1), is related to its high-content multicolor imaging capability[19] with an outstanding balance in terms of time efficiency (sample preparation time and imaging speed), imaging resolution, and cost-effectiveness by enjoying the benefits of the UV surface excitation and real-time labeling. In order to further exploit the spectral information of the color images, computational spectral super-resolution methods[34–36] can be a feasible working

direction, which can generate hyperspectral images with RGB images as the input. To broaden the applications of HiLoTRUST in the life science field, it is vital to explore more types of fluorogenic stains (including aggregation-induced emission-active fluorescent probes[37]), to enrich the imaging capabilities of HiLoTRUST, such as the protein (8-anilino-1-naphthalene sulfonic acid, Sigma-Aldrich) stain and lipids stain (Nile red or DiI, Sigma-Aldrich). However, HiLoTRUST's speckle illumination relies on a single green LD, which poses challenges. Although, as shown in Fig. 4, two adapted HiLo processing pipelines have been proposed to mitigate this issue, the imaging performance is still compromised. To address this, multiple LDs at different wavelengths combined with stains targeting various tissue components can be applied (Supplementary Figure 7). Additionally, a similar setup to the CHAMP system[38], originally designed for super-resolution slide-free imaging, can be adapted for full-color HiLo imaging, where speckle illumination generated by a 266-nm laser is obliquely projected onto the tissue surface (Supplementary Figure 8).

As a proof of concept, although formalin-fixed tumor specimens were imaged, this study is limited by the small number of specimens. To show 3D HiLoTRUST's superiority over 2D histology in clinics, future work covering large amounts of human samples is necessary to quantify the diagnostic metrics (e.g., cancer diagnostic accuracy improvement). Finally, the practicality of HiLoTRUST can be further improved for clinical translations. For example, deep learning-assisted virtual staining could be incorporated with HiLoTRUST to further improve the efficiency of the current pathological workflow[39].

One key superiority of TRUST lies in its rapid whole-organ imaging speed (e.g., ~2 days for an E15 mouse embryo). In comparison to TRUST, the enhanced axial resolution of HiLoTRUST necessitates finer mechanical sectioning, precise focal scanning, and double shots per FOV, consequently multiplying the time required for imaging. To accelerate the acquisition speed, firstly, incorporating more light sources, such as multiple UV-LEDs (e.g., four), and upgrading to a higher-powered UV-LED (M280L, 78 mW, Thorlabs Inc.) from the current model (M285L4, 45 mW, Thorlabs Inc.) could reduce the exposure time. Additionally, using a low-magnification objective lens (e.g., 4×) and a camera with a substantially larger chip size (e.g., PCO Edge 5.5; chip size: 16.64 × 14 mm) can significantly decrease the total number of FOVs. The solution also enhances tolerance to surface roughness due to the increased DOF of the low-magnification objective lens. As for the degraded imaging resolution, it can be recovered with super-resolution neural networks[40] (Supplementary Figure 9). With the aid of deep learning (e.g., pix2pix[41]), it is also possible to achieve single-shot imaging for each FOV in HiLo microscopy (Supplementary Figure 10). Furthermore, unlike the original TRUST system, where the imaging is achieved by translating the whole optical system raster scanning over the tissue surface, the sample is translated instead in the HiLoTRUST system. The much lighter weight makes high-speed mechanical scanning feasible. By updating the current motor (20 mm/s; L-509.x0SD00, PI miCos GmbH) to an advanced model (90 mm/s; L-511, PI miCos GmbH), the motor scanning speed can be enhanced by a factor of five approximately. Finally, regarding the low-speed mechanical axial scanning, extended DOF via dynamic remote focusing[42] holds great promise to speed up the whole imaging process by eliminating the need for axial scanning.

Methods

Sample preparation and processing

Once two mice (wild-type C57BL/6, two months old) were euthanized through five minutes of carbon dioxide inhalation following guidelines provided by the American Veterinary Medical Association, internal organs (e.g., kidney, lung, and liver) were harvested, rinsed with phosphate-buffered saline solution for a minute, and finally fixed by submerging in 10% neutral-buffered formalin (NBF) at room temperature for 24 h. Two human cancer specimens, considered as leftover tissue (i.e., no longer needed for assessment of diagnostic, prognostic, and other parameters in the diagnosis and treatment of the patient), were immediately fixed in formalin for at least 24 h after surgical excision.

Embedding tissue samples in agarose/gelatin contributes to improved sectioning quality. The suggested concentration of agarose or vibratome working parameters should be adjusted based on the tissue type[43]. To section hard specimens (e.g., cancer tissue), 10% (w/v) gelatin embedding with post-fixation by NBF overnight is preferred, as it can tighten the connection between the sample surface and surrounding gelatin after crosslinking[44,45].

Whole-mount staining is not applied in HiLoTRUST. To reduce the labor and time cost for staining, imaged samples will be immersed in staining solutions throughout the experiment for real-time staining[11]. The specimen will be labeled along with image scanning and serial sectioning. To minimize fluorescence background noise from the staining solution itself, we used two of the most common and commercially available fluorogenic stains[20], 4′,6-diamidino-2-phenylindole (DAPI, $\lambda_{Ex}/\lambda_{Em}$: 364/454nm) and propidium iodide (PI, $\lambda_{Ex}/\lambda_{Em}$: 535/615nm) at a concentration of 5 µg/ml, which exhibit increased fluorescence upon binding to cell nuclei.

The human sample protocol was approved by the Institutional Review Board of the University of Hong Kong/Hospital Authority Hong Kong West Cluster (HKU/HA HKW) (reference number: UW20-335) and conforms with the human research ethics protocol approved by the Health, Safety, and Environment Office (HSEO) of The Hong Kong University of Science and Technology (HKUST) (license number: HREP-2021-0270). Informed consent was obtained from all lung cancer tissue donors. All animal experiments were conducted in conformity with the animal protocol approved by the HSEO of the HKUST (license number: AEP-2021-0082).

Basics of HiLo microscopy and resolution measurement

The principles of HiLo microscopy have been extensively discussed, including our recent research on its application for rapid slide-free histological imaging[25]. In brief, two shots are acquired for each FOV: the speckle illumination image (I_s) and the uniform illumination image (I_u). The optical sectioning capability of HiLo microscopy is based on the distinct characteristics of information at different frequencies. In-focus high-frequency components (I_{Hi}) and in-focus low-frequency components (I_{Lo}) are calculated separately and then combined as the final output image (I_{HiLo}). I_{Hi} is naturally in-focus and can be directly extracted by applying a high-pass Gaussian filter on I_u as below:

$$I_{Hi}(\vec{r}) = \mathscr{F}^{-1}\left\{ \mathscr{F}\left[I_u(\vec{r})\right] \times HP\left(\vec{k}\right) \right\} \tag{2}$$

where $\mathscr{F}(\bullet)$ and $\mathscr{F}^{-1}(\bullet)$ denote the Fourier transform and inverse Fourier transform, respectively. $\vec{r}$ and $\vec{k}$ represent the spatial and frequency coordinate, respectively. HP is a high-pass Gaussian filter with a cut-off frequency at k_c. I_{Lo} cannot be extracted simply by applying a complementary low-pass Gaussian filter on I_u (i.e., $\mathscr{F}^{-1}\left\{ \mathscr{F}\left[I_u(\vec{r})\right] \times LP\left(\vec{k}\right) \right\}$), because the processed image results (e.g., Fig. 1e) would still contain out-of-focus information. To address the issue, I_s is needed for evaluating the local focusing status and can effectively eliminate unwanted out-of-focus information. $I_{Lo}(\vec{r})$ can be determined by

$$I_{Lo}(\vec{r}) = \mathscr{F}^{-1}\left\{ \mathscr{F}\left[C_s(\vec{r}) \cdot I_u(\vec{r})\right] \times LP\left(\vec{k}\right) \right\} \tag{3}$$

where the low-pass filter LP is complementary to the high-pass filter HP by $LP\left(\vec{k}\right) = 1 - HP\left(\vec{k}\right)$. Speckle contrast ($C_s$) functions as an object-independent measure of the relative proportion of the uniform illumination image I_u that is in-focus, providing the optical sectioning ability for the low-frequency components of the object and rejecting out-of-focus backgrounds[23]. C_s can be calculated based on the local contrast of the speckle image I_s with the equation below:

$$C_s(\vec{r}) = \frac{sd_\Lambda\left[I_d(\vec{r})\right]}{\mu_\Lambda\left[I_s(\vec{r})\right]} \tag{4}$$

where $sd_\Lambda(\bullet)$ and $\mu_\Lambda(\bullet)$ represent the local standard deviation and local mean value over a square window with a side length of Λ, respectively. Λ can be determined by $\Lambda = 1/2k_c$ to obtain the full spatial spectrum of the object[27]. I_d is the image difference which can be calculated as $I_d(\vec{r}) = I_s(\vec{r}) - I_u(\vec{r})$.

To further accelerate the decay efficiency of $C_s(\vec{r})$ for better axial resolution, band-pass filter BP can be applied to I_d before the calculation of C_s. BP can be generated by subtracting two Gaussian low-pass filters as below:

$$BP\left(\vec{k}\right) = \exp\left(-\frac{|\vec{k}|^2}{2\sigma^2}\right) - \exp\left(-\frac{|\vec{k}|^2}{\sigma^2}\right) \tag{5}$$

where σ is the optical sectioning parameter determining the axial resolution of HiLo microscopy[23,25,46]. Smaller σ although makes a better axial resolution, but at the cost of decreased contrast of C_s (Supplementary Figure 11). Finally, the calculated in-focus high-frequency components (I_{Hi}) and in-focus low-frequency components (I_{Lo}) can be merged as the final output I_{HiLo} by the equation below:

$$I_{HiLo}(\vec{r}) = I_{Hi}(\vec{r}) + \eta \cdot I_{Lo}(\vec{r}) \tag{6}$$

where η is a scaling factor to ensure the seamless transition from the low-pass and high-pass information across the cut-off frequency k_c (approximately equal to 0.18σ[24]). η can be determined experimentally by imaging results[25] or directly calculated based on the equation below at k_c[23].

$$\eta = \frac{\left|\mathscr{F}\left[I_{Hi}(\vec{r})\right]\right|}{\left|\mathscr{F}\left[I_u(\vec{r})\right] \times LP\left(\vec{k}\right)\right|} \tag{7}$$

To quantify the axial resolution R_{axial} of the HiLo microscopy, a specimen by dissolving 10-µm-diameter fluorescent microspheres into 2% w/v melted agarose was prepared. Then, focal scanning over 50 µm with a step size of 1 µm was conducted, with representative results shown in Supplementary Figure 12a–d. The axial intensity distribution curves for multiple fluorescent microsphere beads can be extracted with an averaged Gaussian fitted curve shown in Supplementary Figure 12e. The full width at half maximum (FWHM) was measured as 11.6 µm. Assuming Gaussian-shaped intensity profiles of the beads as well as a Gaussian-shaped point spread function of the microscope, axial resolution R_{axial} was calculated as 5.8 µm based on the equation[25,46] below:

$$R_{axial} = \sqrt{FWHM^2 - d_{bead}^2} \tag{8}$$

where d_{bead} is the average diameter of fluorescent microspheres (i.e., 10 µm).

References

1. Chen, Y. et al. Three-dimensional imaging and quantitative analysis in CLARITY processed breast cancer tissues. *Sci. Rep.* **9**, 5624 (2019).

2. Tanaka, N. et al. Whole-tissue biopsy phenotyping of three-dimensional tumours reveals patterns of cancer heterogeneity. *Nat. Biomed. Eng.* **1**, 796–806 (2017).

3. Ward, J. M., Elmore, S. A. & Foley, J. F. Pathology methods for the evaluation of embryonic and perinatal developmental defects and lethality in genetically engineered mice. *Vet. Pathol.* **49**, 71–84 (2012).

4. Amunts, K. et al. BigBrain: an ultrahigh-resolution 3D human brain model. *Science* **340**, 1472–1475 (2013).

5. Wang, C. W., Budiman Gosno, E. & Li, Y. S. Fully automatic and robust 3D registration of serial-section microscopic images. *Sci. Rep.* **5**, 15051, https://doi.org/10.1038/srep15051 (2015).

6. Ju, T. et al. 3D volume reconstruction of a mouse brain from histological sections using warp filtering. *J. Neurosci. Methods* **156**, 84–100 (2006).

7. Richardson, D. S. & Lichtman, J. W. Clarifying tissue clearing. *Cell* **162**, 246–257 (2015).

8. Richardson, D. S. et al. Tissue clearing. *Nat. Rev. Methods Prim.* **1**, 84 (2021).

9. Ueda, H. R. et al. Tissue clearing and its applications in neuroscience. *Nat. Rev. Neurosci.* **21**, 61–79 (2020).

10. Huisken, J., Swoger, J., Del Bene, F., Wittbrodt, J. & Stelzer, E. H. K. Optical sectioning deep inside live embryos by selective plane illumination microscopy. *Science* **305**, 1007–1009 (2004).

11. Yu, W. et al. Translational rapid ultraviolet-excited sectioning tomography for whole-organ multicolor imaging with real-time molecular staining. *Elife* **11**, 1–21 (2022).

12. Abdeladim, L. et al. Multicolor multiscale brain imaging with chromatic multiphoton serial microscopy. *Nat. Commun.* **10**, 1–14 (2019).

13. Economo, M. N. et al. A platform for brain-wide imaging and reconstruction of individual neurons. *Elife* **5**, e10566, https://doi.org/10.7554/eLife.10566 (2016).

14. Ragan, T. et al. Serial two-photon tomography for automated ex vivo mouse brain imaging. *Nat. Methods* **9**, 255–258 (2012).

15. Wong, T. T. W. et al. Label-free automated three-dimensional imaging of whole organs by microtomy-assisted photoacoustic microscopy. *Nat. Commun.* **8**, 1386 (2017).

16. Seiriki, K. et al. Whole-brain block-face serial microscopy tomography at subcellular resolution using FAST. *Nat. Protoc.* **14**, 1509–1529 (2019).

17. Rodgers, G. et al. Virtual histology of an entire mouse brain from formalin fixation to paraffin embedding. part 1: data acquisition, anatomical feature segmentation, tracking global volume and density changes. *J. Neurosci. Methods* **364**, 109354, https://doi.org/10.1016/j.jneumeth.2021.109354 (2021).

18. Gong, H. et al. Continuously tracing brain-wide long-distance axonal projections in mice at a one-micron voxel resolution. *Neuroimage* **74**, 87–98 (2013).

19. Fereidouni, F. et al. Microscopy with ultraviolet surface excitation for rapid slide-free histology. *Nat. Biomed. Eng.* **1**, 957–966 (2017).

20. Gao, J. et al. Development of fluorogenic probes for rapid high-contrast imaging of transient nuclear localization of sirtuin 3. *ChemBioChem* **21**, 656–662 (2020).

21. Wong, T. T. W. et al. Fast label-free multilayered histology-like imaging of human breast cancer by photoacoustic microscopy. *Sci. Adv.* **3**, e1602168, https://doi.org/10.1126/sciadv.1602168 (2017).

22. Yoshitake, T. et al. Rapid histopathological imaging of skin and breast cancer surgical specimens using immersion microscopy with ultraviolet surface excitation. *Sci. Rep.* **8**, 4476 (2018).

23. Lim, D., Chu, K. K. & Mertz, J. Wide-field fluorescence sectioning with hybrid speckle and uniform-illumination microscopy. *Opt. Lett.* **33**, 1819 (2008).

24. Lim, D., Ford, T. N., Chu, K. K., & Mertz, J. Optically sectioned in vivo imaging with speckle illumination HiLo microscopy. *J. Biomed. Opt.* **16**, 016014 (2011).

25. Zhang, Y., Kang, L., Lo, C. T. K., Tsang, V. T. C. & Wong, T. T. W. Rapid slide-free and non-destructive histological imaging using wide-field optical-sectioning microscopy. *Biomed. Opt. Express* **13**, 2782 (2022).

26. Ventalon, C. & Mertz, J. Dynamic speckle illumination microscopy with translated versus randomized speckle patterns. *Opt. Express* **14**, 7198 (2006).

27. Mazzaferri, J. et al. Analyzing speckle contrast for HiLo microscopy optimization. *Opt. Express* **19**, 14508 (2011).

28. Pelli, D. G. & Bex, P. Measuring contrast sensitivity. *Vision Res* **90**, 10–14 (2013).

29. Schneider, C. A., Rasband, W. S. & Eliceiri, K. W. NIH image to imagej: 25 years of image analysis. *Nat. Methods* **9**, 671–675 (2012).

30. Zhang, Y. J. Handbook of Image Engineering. 1st ed. Springer Singapore 2021, pp 539–559.

31. Mehrvar, S. et al. Three-dimensional vascular and metabolic imaging using inverted autofluorescence. *J. Biomed. Opt.* **26**, 076002 (2021).

32. Staniszewski, K., Audi, S. H., Sepehr, R., Jacobs, E. R. & Ranji, M. Surface fluorescence studies of tissue mitochondrial redox state in isolated perfused rat lungs. *Ann. Biomed. Eng.* **41**, 827–836 (2013).

33. Schindelin, J. et al. Fiji: an open-source platform for biological-image analysis. *Nat. Methods* **9**, 676–682 (2012).

34. Arad, B. et al. NTIRE 2020 Challenge on Spectral Reconstruction from an RGB Image. *IEEE Comput. Soc. Conf. Comput. Vis. Pattern Recognit. Work.* 2020, 1806–1822.

35. Galliani, S., Lanaras, C., Marmanis, D., Baltsavias, E. & Schindler, K. Learned Spectral Super-Resolution. (2017).

36. Li, K., Dai, D. & Van Gool, L. Hyperspectral Image Super-Resolution with RGB Image Super-Resolution as an Auxiliary Task. *Proc. - 2022 IEEE/CVF Winter Conf. Appl. Comput. Vision, WACV 2022* 2022, 4039–4048.

37. Xie, S., Wong, A. Y. H., Chen, S. & Tang, B. Z. Fluorogenic detection and characterization of proteins by aggregation-induced emission methods. *Chem. A Eur. J.* **25**, 5824–5847 (2019).

38. Zhang, Y. et al. High-throughput, label-free and slide-free histological imaging by computational microscopy and unsupervised learning. *Adv. Sci.* **9**, 2102358, https://doi.org/10.1002/advs.202102358 (2022).

39. Kang, L., Yu, W., Zhang, Y., Chen, Z. & Wong, T. T. W. Deep learning enables rapid whole-organ histological imaging with ultraviolet-excited sectioning tomography. *ACS Photonics* **10**, 3541–3550 (2023).

40. Wang, X. et al. ESRGAN: Enhanced Super-Resolution Generative Adversarial Networks. *Lect. Notes Comput. Sci.* **11133 LNCS**, 63–79 (2019).

41. Isola, P., Zhu, J. Y., Zhou, T. & Efros, A. A. Image-to-Image Translation with Conditional Adversarial Networks. In *Proceedings - 30th IEEE Conference on Computer Vision and Pattern Recognition, CVPR 2017*; IEEE, 2017; Vol. 2017-Janua, pp 5967–5976.

42. Shain, W. J., Vickers, N. A., Goldberg, B. B., Bifano, T. & Mertz, J. Extended depth-of-field microscopy with a high-speed deformable mirror. *Opt. Lett.* **42**, 995–998 (2017).

43. *Precisionary | Compresstome Cutting Parameters | Precisionary*. https://www.precisionary.com/cutting-parameters/ (accessed 2021-06-10).

44. Treiber, U., Zwilling, M. & Bayer, E. Crosslinking of gelatin with formaldehyde; a 13C NMR study. *Zeitschrift fur Naturforsch. B.* **41**, 351–358 (1986).

45. Griffioen, H. A., Van der Beek, E. & Boer, G. J. Gelatin embedding to preserve lesion-damaged hypothalami and intracerebroventricular grafts for vibratome slicing and immunocytochemistry. *J. Neurosci. Methods* **43**, 43–47 (1992).

46. Philipp, K. et al. Volumetric HiLo microscopy employing an electrically tunable lens. *Opt. Express* **24**, 15029 (2016).

Author contributions

W.Y. conceived and constructed the HiLoTRUST system. W.Y. conducted experiments to generate the imaging data. Y.Z. created the algorithm for image reconstruction. W.Y. and C.T.K.L. analyzed the findings. L.K. developed the hardware controlling system. W.Y. and T.T.W.W. composed the manuscript. T.T.W.W. oversaw the entire study.

Competing interests

The authors declare no competing interests.

Additional information

Supplementary information The online version contains supplementary material available at https://doi.org/10.1038/s44303-024-00040-4.

Correspondence and requests for materials should be addressed to Terence T. W. Wong.

Reprints and permissions information is available at http://www.nature.com/reprints

Publisher's note Springer Nature remains neutral with regard to jurisdictional claims in published maps and institutional affiliations.